

## Article

# Simultaneous Li-Doping and Formation of SnO<sub>2</sub>-Based Composites with TiO<sub>2</sub>: Applications for Perovskite Solar Cells

Nagisa Hattori <sup>1</sup>, Kazuhiro Manseki <sup>1,\*</sup>, Yuto Hibi <sup>1</sup>, Naohide Nagaya <sup>1</sup>, Norimitsu Yoshida <sup>1</sup>, Takashi Sugiura <sup>1</sup> and Saeid Vafaei <sup>2</sup>

<sup>1</sup> Graduate School of Natural Science and Technology, Gifu University, Yanagido 1-1, Gifu 501-1193, Japan

<sup>2</sup> Mechanical Engineering Department, Bradley University, 1501 West Bradley Avenue, Peoria, IL 61625, USA

\* Correspondence: manseki.kazuhiro.k4@f.gifu-u.ac.jp

**Abstract:** Tin oxide (SnO<sub>2</sub>) has been recognized as one of the beneficial components in the electron transport layer (ETL) of lead-halide perovskite solar cells (PSCs) due to its high electron mobility. The SnO<sub>2</sub>-based thin film serves for electron extraction and transport in the device, induced by light absorption at the perovskite layer. The focus of this paper is on the heat treatment of a nanoaggregate layer of single-nanometer-scale SnO<sub>2</sub> particles in combination with another metal-dopant precursor to develop a new process for ETL in PSCs. The combined precursor solution of Li chloride and titanium(IV) isopropoxide (TTIP) was deposited onto the SnO<sub>2</sub> layer. We varied the heat treatment conditions of the spin-coated films comprising double layers, i.e., an Li/TTIP precursor layer and SnO<sub>2</sub> nanoparticle layer, to understand the effects of nanoparticle interconnection via sintering and the mixing ratio of the Li-dopant on the photovoltaic performance. X-ray diffraction (XRD) and high-resolution transmission electron microscopy (HR-TEM) measurements of the sintered nanoparticles suggested that an Li-doped solid solution of SnO<sub>2</sub> with a small amount of TiO<sub>2</sub> nanoparticles formed via heating. Interestingly, the bandgap of the Li-doped ETL samples was estimated to be 3.45 eV, indicating a narrower bandgap as compared to that of pure SnO<sub>2</sub>. This observation also supported the formation of an SnO<sub>2</sub>/TiO<sub>2</sub> solid solution in the ETL. The utilization of such a nanoparticulate SnO<sub>2</sub> film in combination with an Li/TTIP precursor could offer a new approach as an alternative to conventional SnO<sub>2</sub> electron transport layers for optimizing the performance of lead-halide perovskite solar cells.

**Keywords:** SnO<sub>2</sub>; nanoparticles; solid solution; sintering; solar cells



**Citation:** Hattori, N.; Manseki, K.; Hibi, Y.; Nagaya, N.; Yoshida, N.; Sugiura, T.; Vafaei, S. Simultaneous Li-Doping and Formation of SnO<sub>2</sub>-Based Composites with TiO<sub>2</sub>: Applications for Perovskite Solar Cells. *Materials* **2024**, *17*, 2339. <https://doi.org/10.3390/ma17102339>

Academic Editor: Ioannis Spanopoulos

Received: 10 April 2024

Revised: 2 May 2024

Accepted: 11 May 2024

Published: 14 May 2024



**Copyright:** © 2024 by the authors. Licensee MDPI, Basel, Switzerland. This article is an open access article distributed under the terms and conditions of the Creative Commons Attribution (CC BY) license (<https://creativecommons.org/licenses/by/4.0/>).

## 1. Introduction

In recent years, perovskite solar cells (PSCs) have attracted much attention as a new renewable energy technology [1–5]. They are characterized by a low-cost production process, such as solution deposition, including various printing techniques. This allows for the production of PSCs with fewer installation constraints. Since the initial report on PSCs was published by Miyasaka et al. in 2009 employing the device structure of dye-sensitized solar cells [6], there has been rapid technological innovation in a short period, driven by advancements in variable materials and device structures. Currently, the highest photovoltaic conversion efficiency has reached 26%, rivaling the silicon-based solar cells that are widely used today [7]. The improvement of charge separation and transport efficiencies has been examined by diverse studies employing various electron and hole transport materials. The n-i-p and inverted p-i-n-type device architectures have been developed [8].

The key factor contributing to the improved conversion efficiency of PSCs is the high open-circuit voltage ( $V_{oc}$ ). The elevated  $V_{oc}$  exceeding 1V in organic lead iodide semiconductors, unlike in most dye-sensitized solar cells, arises from minimal voltage loss from the bandgap of perovskite compounds. This characteristic property can suppress

thermal losses due to the charge recombination of electrons and holes. In high-efficiency devices utilizing lead-halide perovskite compounds, direct recombination involving deep traps within the semiconductor bandgap is minimal, while recombination involving shallow traps is considered to dominate the photovoltaic properties. The recombination associated with these shallow traps is mainly influenced by defects occurring at the interfaces between the perovskite crystals and the charge transport layer. Typically, the carrier mobility in the perovskites allows for long diffusion lengths of over 1  $\mu\text{m}$  for electrons and holes. However, recombination related to the mentioned shallow traps is considered to reduce the diffusion length of photoexcited carriers, leading to voltage losses. In other words, suppressing recombination through materials design of charge transport layers contributes to an increase in photovoltaic conversion efficiency [9–14].

The electron transport layer of high-performance n-i-p PSCs often utilizes titanium dioxide ( $\text{TiO}_2$ ) and tin oxide ( $\text{SnO}_2$ ), whereas organic fullerene-based compounds, such as PCBM, were widely used as an electron transport layer in inverted PSCs. For n-i-p PSCs, one advantage of  $\text{SnO}_2$  is its high electron mobility [15].  $\text{SnO}_2$  exhibits a significantly high carrier mobility in the range of 100 to 200  $\text{cm}^2\text{V}^{-1}\text{s}^{-1}$ . Notably, a synergistic effect has been discovered in improving the power conversion efficiency by combining  $\text{SnO}_2$  with  $\text{TiO}_2$  [16–22]. One of the strategies for the electron transport materials includes creating a cascading electron transfer path from the relatively high-conduction band of  $\text{TiO}_2$  to  $\text{SnO}_2$ . Additionally, if an  $\text{SnO}_2$  film surface is covered with a  $\text{TiO}_2$  layer, it is anticipated that the electron transport layer's performance will be enhanced, leading to an improvement in the interface contact with the perovskite layer.

In addition, numerous reports have been reported on PSCs employing metal-doped  $\text{SnO}_2$  materials for electron transport. One of the major advantages was found in the Li-doped electron transport layer, which was prepared by a low-temperature solution process [23]. The downward shift of the conduction band as well as the conductivity enhancement allowed for efficient electron injection and transport and reduced charge recombination. The effects of Li-doping in  $\text{TiO}_2$  have also been developed by several groups in their  $\text{TiO}_2$ -based PSCs (using  $\text{TiO}_2$  solely as an electron transport layer). Li doping has been shown to improve the crystallinity of titanium dioxide and consequently enhance its performance. Additionally, partial reduction of tetravalent titanium to trivalent titanium by doping lithium promotes the passivation of electron defects in the  $\text{TiO}_2$ , leading to performance improvements [24,25].

However, the impact of  $\text{SnO}_2$ , especially with single-nanometer-scale structures, on the process of metal-doping (using post-heating) remains unclear. Moreover, the concept of the creation of nanoparticulate  $\text{SnO}_2$ -based solid-solutions with  $\text{TiO}_2$  has not yet been applied to the metal-doped ETL in PSCs.

In our previous paper [26], we demonstrated the use of phenylalanine methyl ester hydrochloride in the solution synthesis of  $\text{SnO}_2$  nanoaggregates. This allowed us to tune primarily particle sizes to be as small as 3 nm while enhancing the  $\text{SnO}_2$  crystallinity with the assistance of the hydrochloride salt that contributed to promoting the hydrolysis of Sn(IV) sources. In a preliminary experiment, we also showed a spin-coat method to produce a double-layered thin film precursor consisting of the obtained  $\text{SnO}_2$  nanocrystals synthesized at different temperatures (deposited at the bottom) and a TTIP coating layer (deposited on the bottom layer), which were used for the fabrication of PSCs.

Using the  $\text{SnO}_2$  nanoaggregates, we report on the first simultaneous Li-doping and the formation of an  $\text{SnO}_2$  nanoaggregate-based solid solution with a small amount of  $\text{TiO}_2$  nanoparticles. A narrower bandgap as a result of the formation of  $\text{SnO}_2/\text{TiO}_2$  solid solution was also proved as opposed to that of  $\text{SnO}_2$ . We varied the sintering conditions and the mixing ratio of the Li-dopant for the Ti precursor solution to gain insight into the ETL performance of the Li-doped solid solution in PSCs.

## 2. Materials and Methods

### 2.1. Chemicals

L-phenylalanine methyl ester hydrochloride and tin(IV) chloride dihydrate ( $\text{SnCl}_4 \cdot 5\text{H}_2\text{O}$ , >98.0%) were obtained from FUJIFILM Wako Pure Chemical Corporation, Osaka, Japan. Titanium isopropoxide (TTIP, >97%) and lithium chloride ( $\text{LiCl}$ , 99.0%) were purchased from KANTO CHEMICAL Co., Inc., Tokyo, Japan.

Dehydrated solvents, N,N-dimethylformamide (DMF, >99.5%), dimethyl sulfoxide (DMSO, 99.0%), 2-propanol (IPA > 99.7%), and acetonitrile ( $\text{CH}_3\text{CN}$  > 99.5%) were supplied from KANTO CHEMICAL Co., Inc., Tokyo, Japan. Ethanol (99.5%) was from Kanto Chemical Co., Inc., Tokyo, Japan. A Milli-Q<sup>®</sup> integral water purification system (MERCK Ltd., Tokyo, Japan) was used for obtaining  $\text{H}_2\text{O}$  (resistivity:  $18.2 \text{ M}\Omega \cdot \text{cm}$ ). All the chemicals were used as purchased for the experiments.

For the fabrication of perovskite solar cells, lead(II) iodide ( $\text{PbI}_2$ , 99.99%), methylamine hydrobromide (MABr, >98.0%), cesium iodide ( $\text{CsI}$ , >99.0%), formamidinium hydroiodide (FAI, 99.99%), lithium bis(trifluoromethanesulfonyl)imide (Li-TFSI, >98.0%), and formamidinium hydrobromide (FABr, 99.99%) were obtained from TOKYO CHEMICAL INDUSTRY CO., Ltd., Tokyo, Japan. Spiro-MeOTAD, chlorobenzene (CB, 99.8%), and 4-tert-butylpyridine (TBP, 98%) were from SIGMA-ALDRICH, Co., St. Louis, MO, USA.

### 2.2. Preparation of Li-Doped $\text{SnO}_2$ Composites with $\text{TiO}_2$

$\text{SnO}_2$  nanoaggregates were synthesized as follows [26]. After dissolving L-phenylalanine methyl ester hydrochloride (0.43 g) in a mixed solvent of 20 mL of ethanol and water (ethanol:water = 1:1 *v/v*), tin(II) chloride pentahydrate (0.71 g) was added. The solution was stirred at 80 °C for 48 h. After drying the resultant solution in air, 10 mL of ethanol was added to dissolve the mixture. The solution was then spin-coated onto a fluorine-doped tin oxide (FTO) substrate at 3500 RPM for 30 s and then heated at 120 °C for 5 min.

A precursor solution was prepared by mixing ethanol, water, nitric acid, and TTIP. In the case of Li-doping, lithium chloride was dissolved in this solution (Ti:Li = 100:1, 20:1 (mol/mol)). The prepared solution was spin-coated onto the  $\text{SnO}_2$  layer in a two-step process (step 1: 1500 RPM, 30 s, and step 2: 1000 RPM, 60 s). Based on a method previously published by our group [27], it was subsequently heated at 500 °C after preheating at 100 °C in an electric furnace, KDF 300 Plus (DENKEN-HIGHDENTAL, Kyoto, Japan). The strategies for sintering nanoparticles are presented in Figure 1, where the duration times at 500 °C were varied.

The methodology of nanoparticle deposition and subsequent sintering significantly influences the electrical conductivity of the semiconductor nanoparticle layer [28]. For nanoparticle deposition, optimizing the rotating angular velocity (RPM) and deposition duration is crucial to achieving a homogeneous and appropriate thickness of the nano-layer. Similarly, in the case of sintering, the ramping rate, duration at maximum temperature, and the maximum temperature itself play significant roles in determining the porosity of the deposited nanoparticles [29]. Therefore, these parameters need to be optimized to maximize electrical conductivity or electron mobility. As the porosity of deposited semiconductor nanoparticles increases, electrical conductivity decreases, while the interfacial area between semiconductor nanoparticles and light-absorbing materials increases. Hence, porosity must be optimized to enhance the electron mobility of deposited nanoparticles.

In our study, we set the maximum sintering temperature for nanoparticles at 500 °C due to temperature constraints imposed by FTO glasses. Additionally, we varied the duration of sintering to optimize the performance of the solar cell.

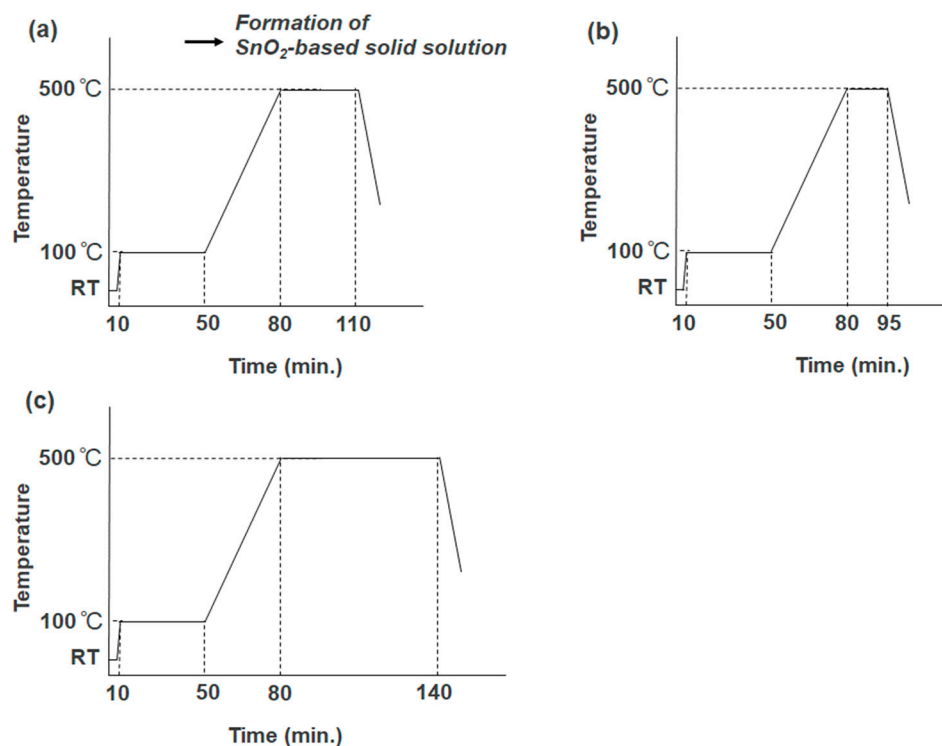


**Figure 1.** Sintering strategies of  $\text{SnO}_2$ -based solid solution with  $\text{TiO}_2$ . The hold times at the maximum temperature of  $500\text{ }^\circ\text{C}$  were (a) 30 min, (b) 15 min, and (c) 1 h, respectively.

### 2.3. Structure Analysis of $\text{SnO}_2/\text{TiO}_2$ Solid-Solution and Their ETL Films

$\text{SnO}_2$ -based solid solution nanoparticles were characterized using X-ray diffraction (XRD, Rigaku RINT Ultima/PC with monochromated  $\text{Cu-K}\alpha$  radiation, Tokyo, Japan). The analysis of the nanostructures was performed by means of TEM (JEM-2100, JEOL, Tokyo, Japan). The diffuse reflectance spectra of the nanoparticles were obtained using a UV-Vis spectrophotometer (V-770, Jasco, Tokyo, Japan). A surface and cross-sectional image of ETL/FTO substrates were obtained using SEM (S-4800, Hitachi High-Tech Corporation, Tokyo, Japan).

### 2.4. Fabrication of Perovskite Solar Cells

We deposited the perovskite layer onto the ETL using a modified process previously reported [30]. All procedures were performed within a glove box filled with nitrogen at a relative humidity of 20%. Prior to the deposition of the perovskite precursor solution, the ETL/FTO substrate was heated to  $80\text{ }^\circ\text{C}$ . The perovskite solution was prepared as follows: CsI (0.07 mmol), FAI (1.19 mmol), MABr (0.14 mmol), and  $\text{PbI}_2$  (1.45 mmol) were dissolved in a mixture of 80 vol% DMF (0.8 mL) and 20 vol% DMSO (0.2 mL). The mixture was stirred for 2 h at  $70\text{ }^\circ\text{C}$  on a hot plate. The substrate was then placed in a spin-coater, and the perovskite solution was dropped onto the substrate with a two-step coating process (1000 RPM for 10 s, followed by 6000 RPM for 30 s). After spin-coating, 300  $\mu\text{L}$  of CB was added. The substrate was further annealed at  $100\text{ }^\circ\text{C}$  for 1 h and then cooled naturally to room temperature. In parallel, FABr (0.12 mmol) was added to 4 mL of IPA to prepare a solution. The FABr solution was coated onto the perovskite layer at 4000 RPM for 20 s, and the substrate was heated at  $80\text{ }^\circ\text{C}$  for 10 min. After heating, the substrate was cooled to room temperature.

A total of 0.045 g of Spiro-MeOTAD was dissolved in 0.5 mL of CB. Separately, 0.052 g of LiTFSI was dissolved in 0.1 mL of acetonitrile. Then, 10  $\mu\text{L}$  of the  $\text{CH}_3\text{CN}$  solution and 17.75  $\mu\text{L}$  of TBP were added to the Spiro-MeOTAD solution. The prepared solution was then spin-coated onto the perovskite layer at 4000 rpm for 20 s. The substrate was removed from the glove box and left to stand in air for 24 h. Finally, a gold counter electrode was deposited

using vacuum evaporation, following the method reported by our group [31]. One-step gold deposition was performed at a pressure of  $2 \times 10^{-3}$  Pa, with the gold layer being deposited by adjusting the source power of the thermal evaporation deposition machine.

### 2.5. Evaluation of Solar Cell Performance

The I–V curves were measured under simulated sunlight ( $100 \text{ mW/cm}^2$ ) using a solar simulator (YSS-80A, Yamashita Denso, Tokyo, Japan) with a potentiostat (HSV-110, Meiden Hokuto, Tokyo, Japan). The active area of the PSCs was  $0.09 \text{ cm}^2$ . Scanning conditions for the I–V measurements were at a scan rate of  $50 \text{ mV/s}$ . A Desktop Spectral Response and IPCE Measurement System (Bunkokeiki SM-250, Tokyo, Japan) was used for the measurement of a spectrum of monochromatic incident photon-to-current conversion efficiency (IPCE).

## 3. Results and Discussions

One of the important steps in preparing ETLs for PSCs involves the sintering process of oxide nanoparticles. The focus should be on how the resultant materials are grown from a precursor solution through conversion via heat treatment. The successive spin-coating and sintering processes of nanoparticles, along with the preparation of the precursor solution, are illustrated in Figure 2. Additionally, the figure presents that an  $\text{SnO}_2$ -based solid solution with  $\text{TiO}_2$  can be formed. Moreover, we anticipate that the additional process of depositing an Li-containing titanium(IV) isopropoxide (TTIP) solution on top of a nanostructured  $\text{SnO}_2$  bottom layer could provide a beneficial platform for realizing effective metal doping in the  $\text{SnO}_2$  core during heat treatment. This approach could offer a favorable method for optimizing electron transport in thin films in PSCs.

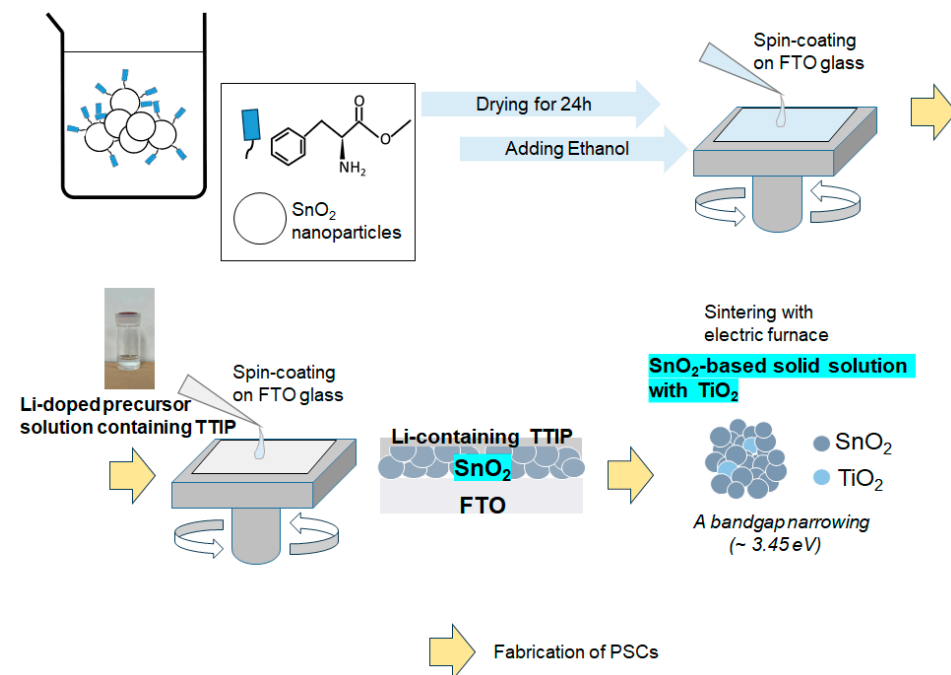


**Figure 2.** Schematics of the formation of  $\text{SnO}_2$ -based solid solution with  $\text{TiO}_2$  as an electron transport layer in perovskite solar cells.  $\text{SnO}_2$  nanoaggregates were synthesized using our structure directing agent (SDA)-supported hydrolysis method, previously reported in [26]. In the final step of ETL preparation, sintering at  $500 \text{ }^\circ\text{C}$  produced the Li-doping  $\text{SnO}_2$ -based solid solution with  $\text{TiO}_2$ , followed by the deposition of the lead-halide perovskite layer on top of the ETL. Annealing steps (drying process) after the two spin-coating were omitted for clarity. A bandgap narrowing of  $\text{SnO}_2$  nanoparticles induced by  $\text{TiO}_2$  nanoparticles was observed.

Structural investigation of sintered oxide nanoparticles in ETLs is crucial for understanding the growth mechanism of the resultant solid solution from the mixed system of SnO<sub>2</sub> and Ti(IV) sources. However, microstructural analysis, especially of the sintered ETL, has not been well conducted. This was achieved particularly using a high-resolution transmission electron microscope (TEM), as discussed below. Sintering plays a significant role in controlling the crystal growth of nanoparticles. It is important to determine optimized heat-treatment conditions of ETLs, considering changes in several factors such as maximum temperatures, hold times at the temperatures, and ramping rates of heating. We systematically investigated the sintering conditions at 500 °C, while varying the periods of maximum temperature. Additionally, the Li-dopant rate was varied to understand the effects of doping on the photovoltaic properties.

Figure 3 displays the XRD patterns of the sintered SnO<sub>2</sub> samples. For Figure 3a–d, the Li-dopant rates for the TTIP solution were 1 mol% and 5 mol%, and hold times during heating at 500 °C were 30 min and 1 h. As a control, non-doped samples are also measured and presented in Figure 3e,f. All observed peaks were assigned to rutile TiO<sub>2</sub> and SnO<sub>2</sub> only, indicating that the heating process at 500 °C resulted in the incorporation of TiO<sub>2</sub> into SnO<sub>2</sub>. No other impurities, such as Li and its oxides, were detected when the doping concentration was increased, suggesting that the TiO<sub>2</sub> or SnO<sub>2</sub> crystal lattice were partially replaced by a Li ion with a similar ionic radius and defect formation was suppressed. Regarding hold times at maximum temperature during heating, cracks on the TiO<sub>2</sub> or SnO<sub>2</sub> surface increased with increasing time.

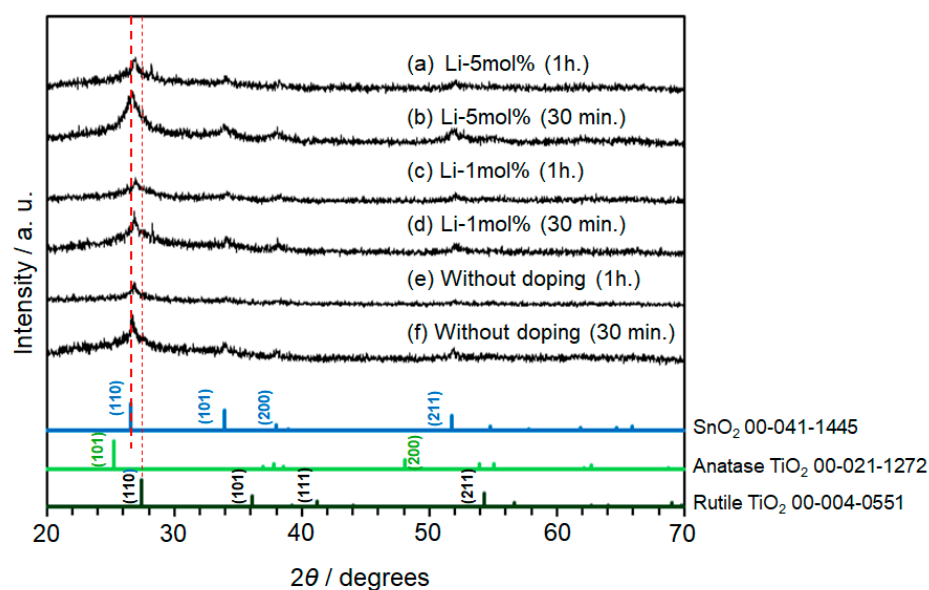


**Figure 3.** XRD patterns of the sintered samples of SnO<sub>2</sub>-based solid solution with TiO<sub>2</sub> are shown in (a–d). Non-doped samples are presented as a control experiment in (e,f). The database of SnO<sub>2</sub> and TiO<sub>2</sub> (anatase and rutile) is also provided at the bottom. For the XRD patterns in (a–d), the Li-dopant rates were 1 mol% and 5 mol%, and the hold time of heating were 30 min and 1 h. Red dotted lines are shown for clarity.

Notably, the peak intensity increased with increasing Li concentration in the precursor solution for Li-5 mol% samples, leading to improved crystallinity. Using the Scherrer equation, the crystallite size in each sample was calculated as shown in Table 1. In fact, the calculated crystallite sizes increased when the doping rate was high, while the opposite trend was observed for samples sintered for 1 h. The results suggest that the hold time during sintering is a decisive factor in adjusting the growth of nanoparticles.

**Table 1.** Calculated crystallite sizes of sintered SnO<sub>2</sub> nanoparticles. The crystallite sizes of the nanoparticles were estimated using the Scherrer equation \*.

ETLs	Hold Times in Heating	Calculated Crystallite Sizes (nm)
Without doping	30 min.	2
Without doping	1 h.	11
Li-1mol%	30 min.	2
Li-1mol%	1 h.	7
Li-5mol%	30 min.	4
Li-5mol%	1 h.	5

\*  $D = K\lambda / \beta \cos \theta$ , D, K,  $\lambda$ , and  $\theta$  show the crystallite size, Scherrer constant (0.90), X-ray wavelength (1.54 Å), and Bragg angle, respectively.

To investigate the influence of Li doping on the morphology of ETLs, we carried out the scanning electron microscope (SEM) to observe the undoped and Li-doped films. As shown in Figure 4, these SEM images show that the morphologies of the films were not affected by Li doping. It was also observed that a dense and smooth layer without pinholes was formed. Cross-sectional SEM images showed that the thickness of both thin films was about 50–100 nm, with particle sizes ranging from 10 to 30 nm. The film thickness is very thin, and the surface SEM image shows some uneven structure of the FTO, which is thought to indicate that the surface of the FTO is not completely covered.

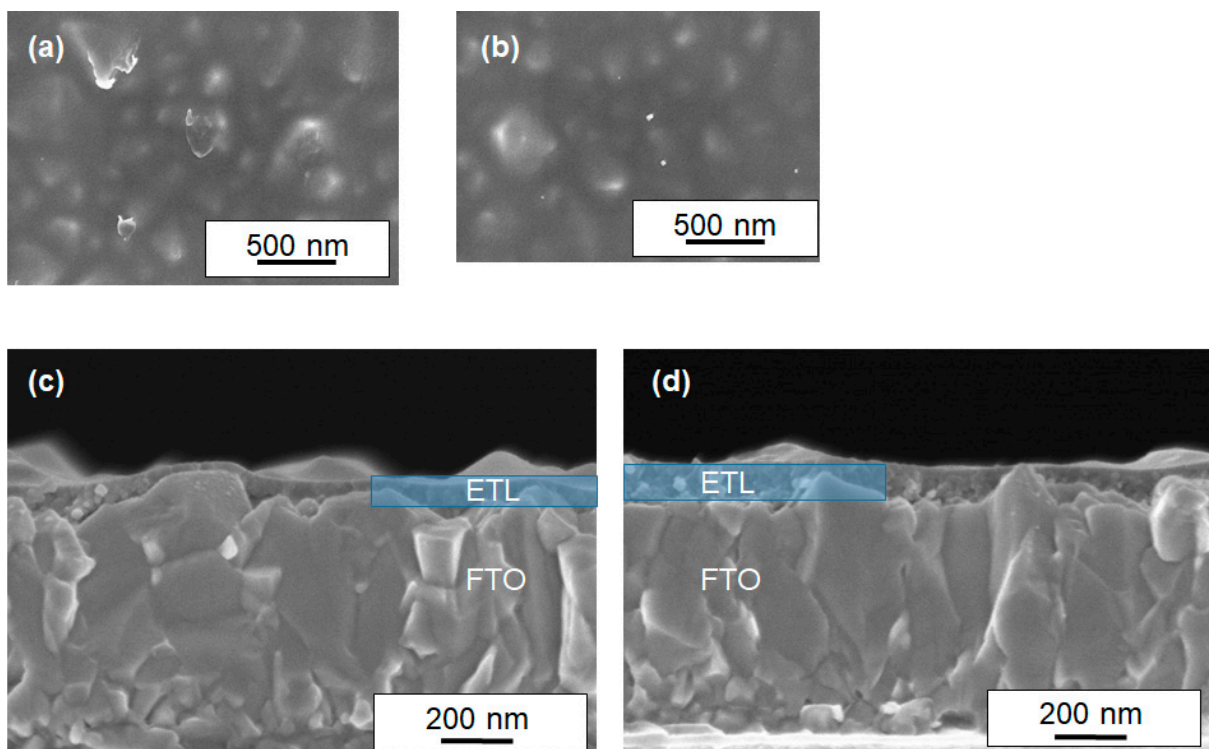


**Figure 4.** SEM images of the sintered samples of SnO<sub>2</sub>-based solid solution with TiO<sub>2</sub> are provided. Non-doped samples (a,c) and Li-doped (5 mol%, b,d) samples are presented. Images (a,b) depict the surface of the films, while (c,d) show cross-sectional images of the ETL/FTO substrates. The ETL layers are highlighted in blue.

TEM measurements provide a straightforward insight into the formation of the SnO<sub>2</sub>-based solid solution. Figure 5 shows TEM images of an SnO<sub>2</sub>-based solid solution with TiO<sub>2</sub> (Li-5 mol%, 30 min sintering). Figure 5a,b depicts the bright-field image of the sintered nanoparticles and the selected area diffraction (SAD) pattern of the same position, respectively. It turned out that the diffraction spots of both TiO<sub>2</sub> and SnO<sub>2</sub> were of (110)

crystal planes. Along with the result, high-resolution images of (Figure 5c,d) clearly indicated the formation of rutile  $\text{TiO}_2$  and  $\text{SnO}_2$  nanoparticles, with approximate crystal sizes of 5 nm. The dimensions of the crystals were in agreement with the calculated data shown in Table 1. The estimated  $d$ -spacings for the observed nanoparticles were 0.32 nm for  $\text{TiO}_2$  and 0.34 nm for  $\text{SnO}_2$ , which are consistent with the SAD pattern.

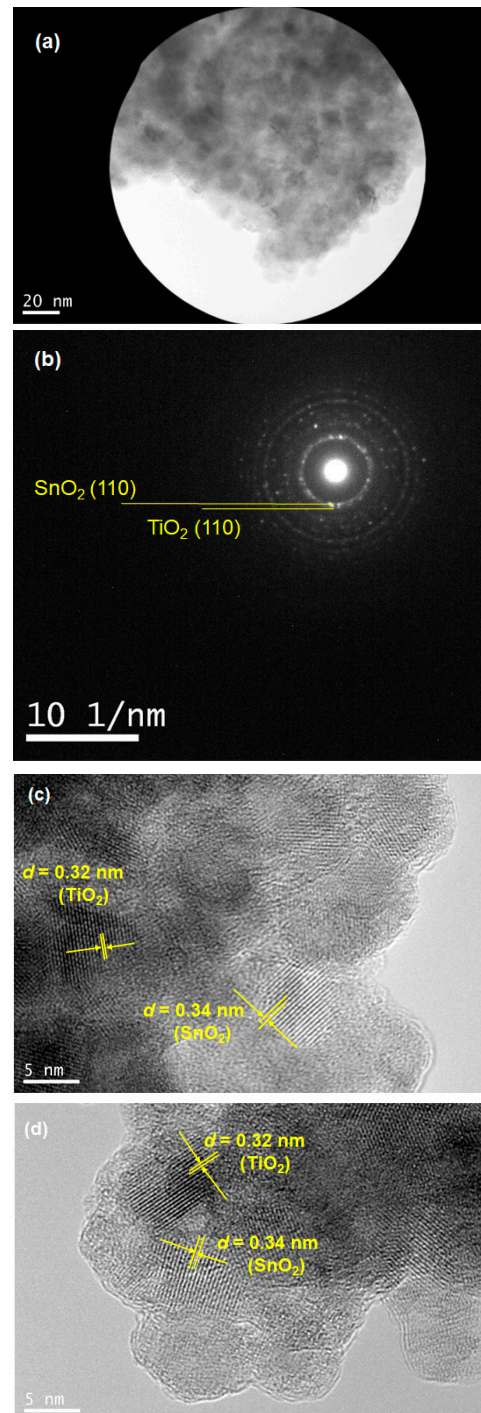


**Figure 5.** TEM images of the  $\text{SnO}_2$ -based solid solution with  $\text{TiO}_2$  (Li-5 mol%) are presented. Images (a,b) show the sintered nanoparticle and its corresponding selected area diffraction (SAD) pattern (scale bar in (b):  $10 \text{ nm}^{-1}$ ), respectively. Images (c,d) are high-resolution images observed at different positions. D-spacings of both  $\text{TiO}_2$  and  $\text{SnO}_2$  for (c,d) are also presented.

Figure 6 also presents data for an SnO<sub>2</sub>-based solid solution with TiO<sub>2</sub> (Li-1 mol%, 30 min sintering). The SAD ring pattern was also observed, as shown in Figure 6b. The location highlighted in yellow in Figure 6a corresponds to the high-resolution image of Figure 6c. D-spacings of the lattice fringes were assigned to be 0.32 nm for TiO<sub>2</sub> and 0.33 nm for SnO<sub>2</sub>, similar to those of the Li-5 mol% data. It was also confirmed that the observed crystal sizes, as small as 5 nm, were consistent with the calculated data. As a result of the heating process at 500 °C, the TEM images in Figures 5 and 6 clearly indicate that nanoparticles were densely packed to form a solid solution of SnO<sub>2</sub>/TiO<sub>2</sub> due to sintering effects.

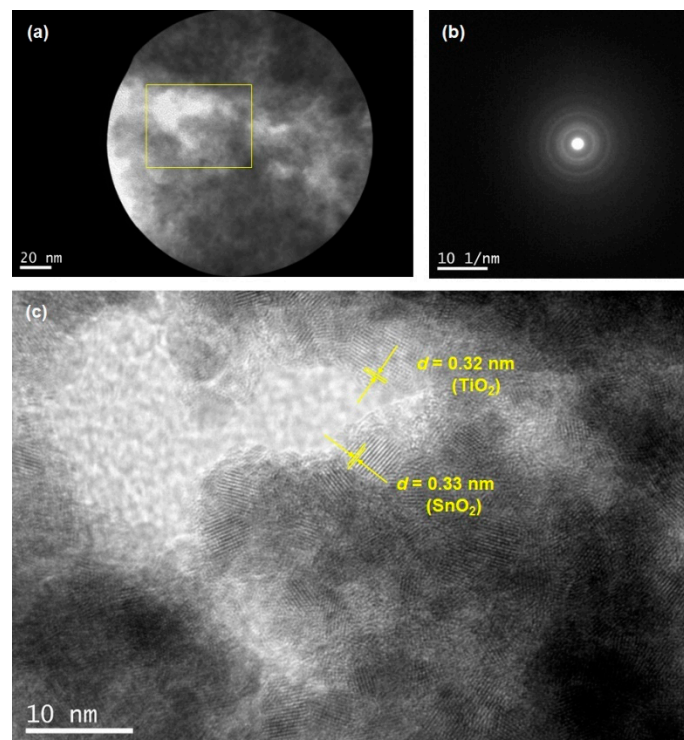


**Figure 6.** TEM images of the SnO<sub>2</sub>-based solid solution with TiO<sub>2</sub> (Li-1 mol%) are provided. Images (a,b) display the sintered nanoparticle and its corresponding SAD pattern (scale bar in (b): 10 nm<sup>-1</sup>), respectively. Image (c) is a high-resolution image corresponding to the location highlighted in yellow in image (a). D-spacings of both TiO<sub>2</sub> and SnO<sub>2</sub> are also presented.

The bandgap of the Li-doped samples (Li-1 mol% and 5 mol%) was estimated to be 3.45 eV for both samples from the diffuse reflection spectra, as shown in Figure 7, irrespective of the Li doping concentration. The bandgap of SnO<sub>2</sub> is known to be 3.6 eV [32]. It should be noted that the bandgap of their Li-doped samples is considered to be narrowed due to the formation of the solid solution of SnO<sub>2</sub> and TiO<sub>2</sub>.

To understand the effective Li-doping conditions in ETLs, eighteen different processes were tested to evaluate the performance of the ETLs. Different hold times in the sintering and Li-doping rates were examined. The representative I–V curves for the 30 min sintering were depicted in Figure 8, and all the I–V parameters were summarized in Tables 2 and 3. Most notably, Li-doping played a significant role in suppressing hysteresis behavior (hysteresis index: HI < 1%), as shown in Table 2. Several groups have reported a similar observation of low HI induced by Li-doping [33]. The hysteresis index was calculated, based on PCE values measured in forward and reverse scans [34]. However, this trend was observed only for the 30 min sintering. It was found that the hold times in the sintering are important factors for determining the photovoltaic performance. There are some reports on Li-doping that can assist in passivating the defects in the TiO<sub>2</sub> and SnO<sub>2</sub> films, increasing the conductivity of metal oxides [35,36]. In addition, relatively larger V<sub>oc</sub> and FF values were observed for the Li-doped samples (Li-1 mol% and 5 mol%) heated for 30 min, leading

to an improvement in PCEs. These results can likely be explained by the simultaneous effects of Li-doping and optimized sintering conditions (30 min) of nanoparticles. It is probable that the smaller crystallite sizes of nanoparticles, as shown in Table 1, have an advantage in the enhancement of sintering, allowing for the formation of favored electron transport layers.

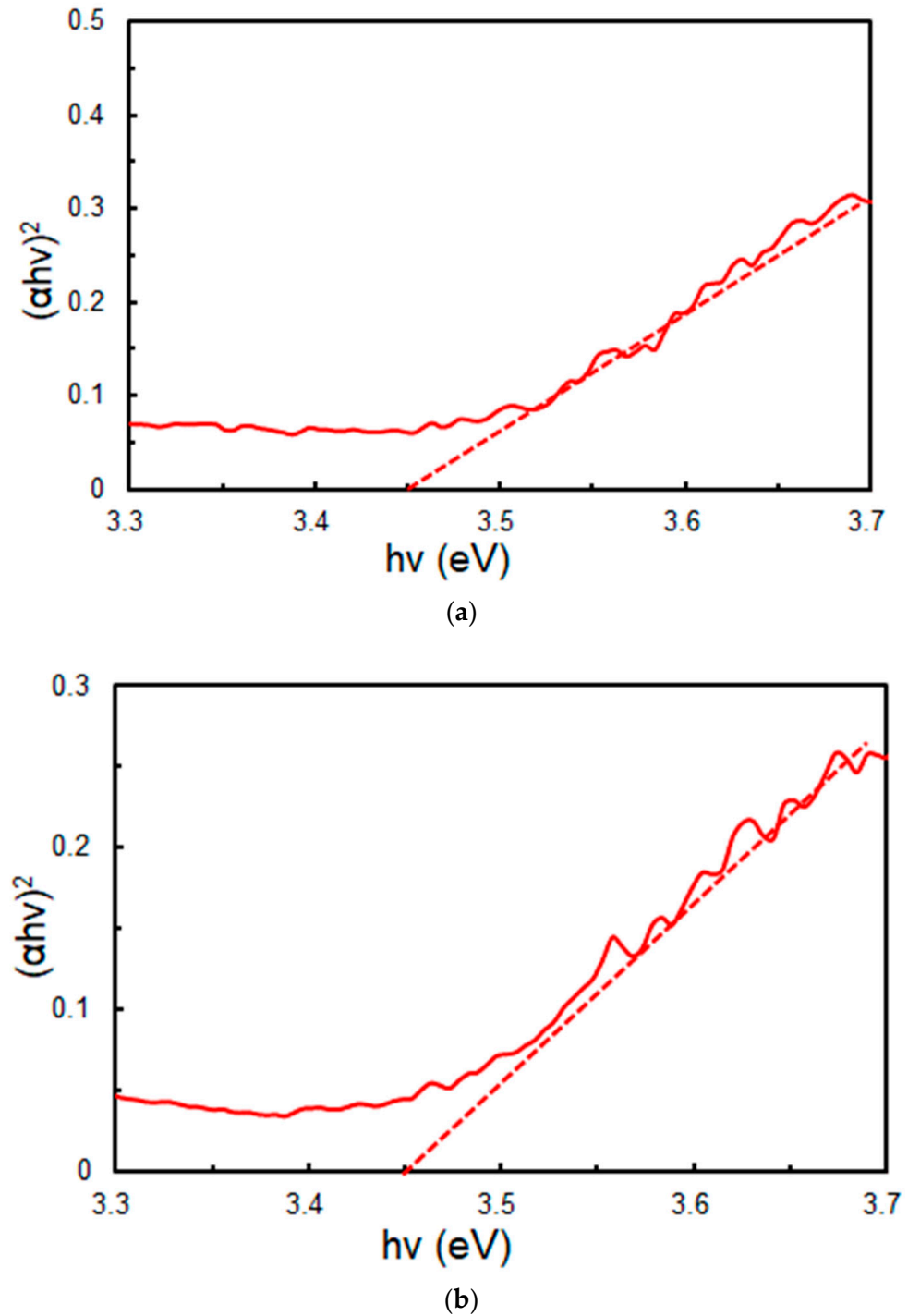


**Figure 7.** Bandgap estimation of Li-doped SnO<sub>2</sub>-based solid solution ETLs (red solid lines): (a) 1 mol% (b) 5 mol%. The linear parts of these Tauc plot are extrapolated to the X-axis using red dotted lines. The ETLs were sintered at 500 °C for 30 min.

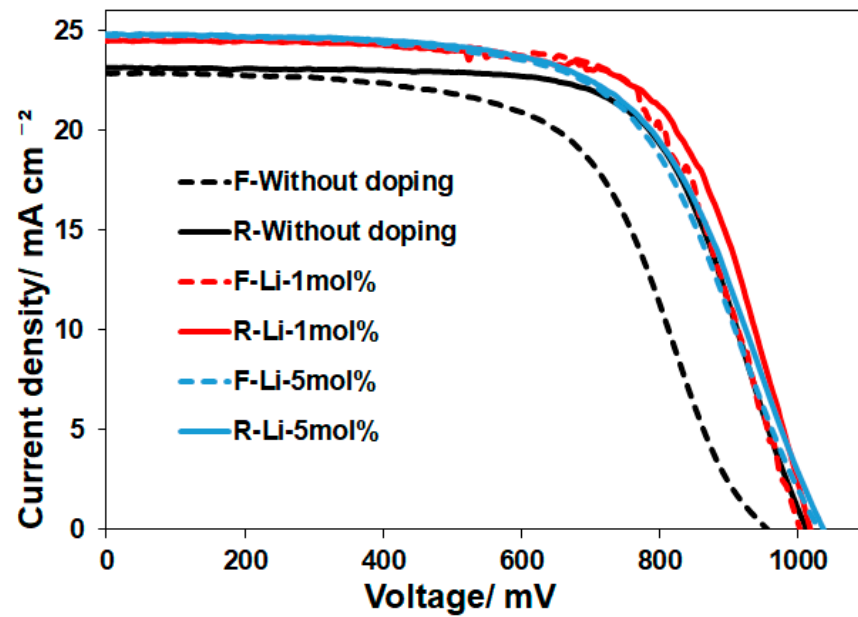


**Figure 8.** I–V curves of PSCs prepared with the ETLs of Li-doped SnO<sub>2</sub>-based solid solutions. The measurements were conducted under simulated sunlight (100 mW/cm<sup>2</sup>). The data were obtained by reverse (R) and forward scans (F).

**Table 2.** I–V parameters of the PSCs with sintered Li-doped ETLs. All the data were obtained by reverse and forward scans. The hold time at the maximum temperature in the sintering was 30 min. The decreased hysteresis index (HI) of I–V curves induced by Li-doping is also indicated by a red arrow.

	V <sub>oc</sub> (mV)	J <sub>sc</sub> (mA/cm <sup>2</sup> )	FF	PCE (%)	HI (%)
Without doping (Reverse: R) (30 min.)	1015	23.1	0.67	15.8	17.1
Without doping (Forward: F) (30 min.)	956	22.9	0.60	13.1	↓
R-Li-1mol% (30 min.)	1027	24.5	0.68	17.0	0.59
F-Li-1mol% (30 min.)	1002	24.6	0.68	16.9	
R-Li-5mol% (30 min.)	1041	24.8	0.62	16.0	1.25
F-Li-5mol% (30 min.)	1030	24.8	0.62	15.8	

**Table 3.** I–V parameters of the PSCs with sintered Li-doped ETLs. The hold time at the maximum temperature in the sintering was 15 min and 1 h. The hysteresis index (HI) of I–V curves is also presented.

	V <sub>oc</sub> (mV)	J <sub>sc</sub> (mA/cm <sup>2</sup> )	FF	PCE (%)	HI (%)
R-Without doping (15 min.)	759	23.8	0.63	11.4	4.4
F-Without doping (15 min.)	725	23.8	0.63	10.9	
R-Without doping (1 h.)	995	23.8	0.60	14.2	5.6
F-Without doping (1 h.)	960	23.8	0.57	13.0	
R-Li-1mol% (15 min.)	936	24.8	0.56	12.9	16.3
F-Li-1mol% (15 min.)	887	24.8	0.49	10.8	

Table 3. Cont.

	$V_{oc}$ (mV)	$J_{sc}$ (mA/cm <sup>2</sup> )	FF	PCE (%)	HI (%)
R-Li-1mol% (1 h.)	1038	23.3	0.63	15.3	13.1
F-Li-1mol% (1 h.)	980	24.1	0.56	13.3	
R-Li-5mol% (15 min.)	997	25.0	0.55	13.8	16.0
F-Li-5mol% (15 min.)	963	24.8	0.48	11.6	
R-Li-5mol% (1 h.)	1031	24.2	0.62	15.5	5.2
F-Li-5mol% (1 h.)	1002	24.4	0.60	14.7	

To confirm the ability of the perovskite compound to convert light into electrical energy, we conducted measurements of incident photon-to-current conversion efficiency (IPCE). Figure 9 illustrates the IPCE response obtained from a sintered Li-doped ETL (1 mol%)-based PCE, which demonstrated the best performance in this study. The results indicate that a significant portion of visible light and near-infrared radiation, up to approximately 850 nm, can be efficiently converted into electricity. This corresponds to the light absorption characteristics of the lead-halide perovskite compound in the device. Based on the cross-sectional SEM images in Figure 4, it is evident that the partial contact between the perovskite and FTO should be minimized by further adjusting the thickness of the ETLs. This is crucial, as partial contact between the perovskite and FTO can induce charge recombination in the device. Optimization of the device is currently underway by varying the film thickness of the ETLs.

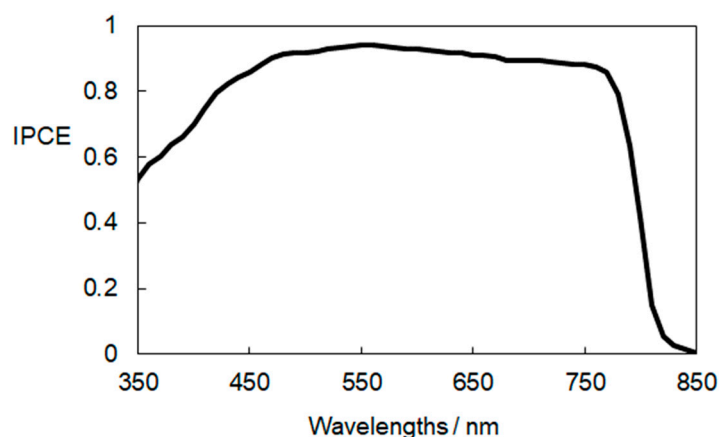


Figure 9. IPCE spectrum of the best-performing PSC with a sintered Li-1 mol% ETL. The hold time at 500 °C in the sintering was 30 min.

#### 4. Conclusions

We have demonstrated that the sintering of the integrated double layers, i.e., a layer of single-nanometer-scale SnO<sub>2</sub> particles and Li-containing TTIP precursors, enabled the production of Li-doped SnO<sub>2</sub>-based solid solution with TiO<sub>2</sub>, which can be processed with a thickness of 50–100 nm. The combined precursor of lithium chloride and TTIP facilitated effective metal doping via heating in the resultant oxide thin films. Notably, the bandgap of the Li-doped ETL samples was estimated to be 3.45 eV, indicating a narrower bandgap as compared to that of pure SnO<sub>2</sub> (3.6 eV). Also, hold time in the sintering was found to be a crucial factor determining the performance of PSCs. We varied the heat treatment conditions while changing the mixing ratio of the Li-dopant. The nanostructures of the resultant solid

solution materials were successfully characterized using XRD and HR-TEM measurements. Successive spin-coating and sintering that can convert the integrated double layers into a doped SnO<sub>2</sub>-based solid solution as an ETL could offer a beneficial approach as an alternative to conventional SnO<sub>2</sub> ETLs for high-efficiency lead-halide perovskite solar cells.

**Author Contributions:** Conceptualization, S.V. and K.M.; methodology, S.V. and K.M.; formal analysis, N.H., Y.H., N.N., N.Y., T.S. and K.M.; film deposition and solar cells fabrication, N.H., Y.H. and N.N.; writing—original draft preparation, S.V. and K.M.; writing—review and editing, S.V. and K.M.; project administration; K.M. All authors have read and agreed to the published version of the manuscript.

**Funding:** The author (K.M.) acknowledges the support from General Incorporated Foundation International Club (Research and Education Grant Program) and JSPS KAKENHI Grant Number JP23H02003.

**Institutional Review Board Statement:** Not applicable.

**Informed Consent Statement:** Not applicable.

**Data Availability Statement:** Data are contained within the article.

**Conflicts of Interest:** The authors declare no conflicts of interest.

## References

1. Jena, A.K.; Kulkarni, A.; Miyasaka, T. Halide perovskite photovoltaics: Background, status, and future prospects. *Chem. Rev.* **2019**, *119*, 3036–3103. [[CrossRef](#)] [[PubMed](#)]
2. Hussain, I.; Tran, H.P.; Jaksik, J.; Moore, J.; Islam, N.; Uddin, M.J. Functional materials, device architecture, and flexibility of perovskite solar cell. *Emergent Mater.* **2018**, *1*, 133–154. [[CrossRef](#)]
3. George, J.; Joseph, A.P.; Balachandran, M. Perovskites: Emergence of highly efficient third-generation solar cells. *Int. J. Energy Res.* **2022**, *46*, 21856–21883. [[CrossRef](#)]
4. Basumatary, P.; Agarwal, P. A short review on progress in perovskite solar cells. *Mater. Res. Bull.* **2022**, *149*, 111700. [[CrossRef](#)]
5. Ramanathan, R.; Mallik, R.C.; Zinigrad, M. Effective Approaches for Perovskite Solar Cells: Recent Advances and Perspectives. *Phys. Status Solidi A* **2023**, *220*, 2300091. [[CrossRef](#)]
6. Kojima, A.; Teshima, K.; Shirai, Y.; Miyasaka, T. Organometal halide perovskites as visible-light sensitizers for photovoltaic cells. *J. Am. Chem. Soc.* **2009**, *131*, 6050–6051. [[CrossRef](#)] [[PubMed](#)]
7. He, J.; Wang, S.; Li, X.; Zhang, F. Seeding Agents in Metal Halide Perovskite Solar Cells: From Material to Mechanism. *ChemSusChem* **2023**, *16*, e202202109. [[CrossRef](#)] [[PubMed](#)]
8. Fakharuddin, A.; Armadorou, K.-K.; Zorba, L.P.; Tountas, M.; Seewald, T.; Soultati, A.; Tsipas, P.; Schütz, E.R.; Tzoganakis, N.; Panagiotakis, S.; et al. A Triethyleneglycol C60 Mono-adduct Derivative for Efficient Electron Transport in Inverted Perovskite Solar Cells. *Chin. J. Chem.* **2023**, *41*, 431–442. [[CrossRef](#)]
9. Shao, S.; Loi, M.A. The Role of the Interfaces in Perovskite Solar Cells. *Adv. Mater. Interfaces* **2020**, *7*, 1901469. [[CrossRef](#)]
10. Mahjabin, S.; Haque, M.; Sobayel, K.; Jamal, M.S.; Islam, M.A.; Selvanathan, V.; Assaifan, A.K.; Alharbi, H.F.; Sopian, K.; Amin, N.; et al. Perceiving of Defect Tolerance in Perovskite Absorber Layer for Efficient Perovskite Solar Cell. *IEEE Access* **2020**, *8*, 106346–106353. [[CrossRef](#)]
11. Wang, F.; Bai, S.; Tress, W.; Hagfeldt, A.; Gao, F. Defects engineering for high-performance perovskite solar cells. *NPJ Flex. Electron.* **2018**, *2*, 22. [[CrossRef](#)]
12. Aydin, E.; De Bastiani, M.; De Wolf, S. Defect and Contact Passivation for Perovskite Solar Cells. *Adv. Mater.* **2019**, *31*, 1900428. [[CrossRef](#)] [[PubMed](#)]
13. Liu, J.; Li, S.; Mei, A.; Han, H. Applications of Metal Oxide Charge Transport Layers in Perovskite Solar Cells. *Small Sci.* **2023**, *3*, 2300020. [[CrossRef](#)]
14. Valadi, K.; Gharibi, S.; Taheri-Ledari, R.; Akin, S.; Maleki, A.; Shalan, A.E. Metal oxide electron transport materials for perovskite solar cells: A review. *Environ. Chem. Lett.* **2021**, *19*, 2185–2207. [[CrossRef](#)]
15. Sharma, H.; Srivastava, R. Solution-processed pristine metal oxides as electron-transporting materials for perovskite solar cells. *Front. Electron. Mater.* **2023**, *3*, 1174159. [[CrossRef](#)]
16. Li, N.; Yan, J.; Ai, Y.; Jiang, E.; Lin, L.; Shou, C.; Yan, B.; Sheng, J.; Ye, J. A low-temperature TiO<sub>2</sub>/SnO<sub>2</sub> electron transport layer for high-performance planar perovskite solar cells. *Sci. China Mater* **2020**, *63*, 207–215. [[CrossRef](#)]
17. Ko, Y.; Kim, T.; Lee, C.; Lee, C.; Yun, Y.J.; Jun, Y. Alleviating Interfacial Recombination of Heterojunction Electron Transport Layer via Oxygen Vacancy Engineering for Efficient Perovskite Solar Cells Over 23%. *Energy Environ. Mater.* **2023**, *6*, e12347. [[CrossRef](#)]
18. Lee, J.; Kim, J.; Kim, C.S.; Jo, S. Compact SnO<sub>2</sub>/mesoporous TiO<sub>2</sub> Bilayer Electron Transport Layer for Perovskite Solar Cells Fabricated at Low Process Temperature. *Nanomaterials* **2022**, *12*, 718. [[CrossRef](#)]
19. Chen, D.; Su, A.; Li, X.; Pang, S.; Zhu, W.; Xi, H.; Chang, J.; Zhang, J.; Zhang, C.; Hao, Y. Efficient planar perovskite solar cells with low-temperature atomic layer deposited TiO<sub>2</sub> electron transport layer and interfacial modifier. *Sol. Energy* **2019**, *188*, 239–246. [[CrossRef](#)]

20. Hu, M.; Zhang, L.; She, S.; Wu, J.; Zhou, X.; Li, X.; Wang, D.; Miao, J.; Mi, G.; Chen, H.; et al. Electron Transporting Bilayer of SnO<sub>2</sub> and TiO<sub>2</sub> Nanocolloid Enables Highly Efficient Planar Perovskite Solar Cells. *Sol. RRL* **2020**, *4*, 1900331. [[CrossRef](#)]
21. Shu, H.; Peng, C.; Chen, Q.; Huang, Z.; Deng, C.; Luo, W.; Huang, Y. Strategy of Enhancing Built-in Field to Promote the Application of C-TiO<sub>2</sub>/SnO<sub>2</sub> Bilayer Electron Transport Layer in High-Efficiency Perovskite Solar Cells (24.3%). *Small* **2022**, *18*, 2204446. [[CrossRef](#)] [[PubMed](#)]
22. Liu, Q.; Fei, F.; Xu, Y.; Gu, L.; Ding, X.; Wang, K.; Du, K.; Wang, S.; Dong, X.; Li, L.; et al. SnO<sub>2</sub>: TiO<sub>2</sub> hybrid nanocrystals as electron transport layer for high-efficiency and stable planar perovskite solar cells. *Org. Electron.* **2023**, *120*, 106815. [[CrossRef](#)]
23. Park, M.; Kim, J.-Y.; Son, H.J.; Lee, C.-H.; Jang, S.S.; Ko, M.J. Low-temperature solution-processed Li-doped SnO<sub>2</sub> as an effective electron transporting layer for high-performance flexible and wearable perovskite solar cells. *Nano Energy* **2016**, *26*, 208–215. [[CrossRef](#)]
24. Zhao, F.; Guo, Y.; Yang, P.; Tao, J.; Jiang, J.; Chu, J. Effect of Li-doped TiO<sub>2</sub> layer on the photoelectric performance of carbon-based CsPbIBr<sub>2</sub> perovskite solar cell. *J. Alloy Compd.* **2023**, *930*, 167377. [[CrossRef](#)]
25. Teimouri, R.; Heydari, Z.; Ghaziani, M.P.; Madani, M.; Abdy, H.; Kolahtouz, M.; Asl-Soleimani, E. Synthesizing Li doped TiO<sub>2</sub> electron transport layers for highly efficient planar perovskite solar cell. *Superlattices Microstruct.* **2020**, *145*, 106627. [[CrossRef](#)]
26. Hattori, N.; Vafaei, S.; Narita, R.; Nagaya, N.; Yoshida, N.; Sugiura, T.; Manseki, K. Growth and dispersion control of SnO<sub>2</sub> nanocrystals employing an amino acid ester hydrochloride in solution synthesis: Microstructures and photovoltaic applications. *Materials* **2023**, *16*, 7649. [[CrossRef](#)] [[PubMed](#)]
27. Vafaei, S.; Boddu, V.K.; Jala, S.; Bezawada, P.K.; Hattori, N.; Higashi, S.; Sugiura, T.; Manseki, K. Preparation of Nanostructured Sn/Ti Oxide Hybrid Films with Terpeneol/PEG-Based Nanofluids: Perovskite Solar Cell Applications. *Materials* **2023**, *16*, 3136. [[CrossRef](#)] [[PubMed](#)]
28. Vafaei, S.; Holmes, I.; Errion, B.; Thukka, Z.; Narita, R.; Sugiura, T.; Manseki, K. Manufacturing a TiO<sub>2</sub>-based semiconductor film with nanofluid pool boiling and sintering processes toward solar-cell applications. *Nanomaterials* **2022**, *12*, 1165. [[CrossRef](#)] [[PubMed](#)]
29. Vafaei, S.; Thomas, D.; Wolosz, A.; Manseki, K.; Sugiura, T. Sintering strategies for creating 3D TiO<sub>2</sub> nanomaterials for photovoltaic applications. In Proceedings of the Thermal and Fluids Engineering Summer Conference, Virtual, 26–28 May 2021; pp. 1305–1313.
30. Suo, J.; Yang, B.; Mosconi, E.; Choi, H.S.; Kim, Y.; Zakeeruddin, S.M.; De Angelis, F.; Grätzel, M.; Kim, H.S.; Hagfeldt, A. Surface reconstruction engineering with synergistic effect of mixed-salt passivation treatment toward efficient and stable perovskite solar cells. *Adv. Funct. Mater.* **2021**, *31*, 2102902. [[CrossRef](#)]
31. Manseki, K.; Yamasaki, M.; Yoshida, N.; Sugiura, T.; Vafaei, S. Optimization of thermal evaporation process of gold deposition for perovskite solar cells. In Proceedings of the Thermal and Fluids Engineering Summer Conference, New Orleans, LA, USA, 5–8 April 2020; pp. 739–745.
32. Gutierrez, G.; Sundin, E.M.; Nalam, P.G.; Zade, V.; Romero, R.; Nair, A.N.; Sreenivasan, S.; Das, D.; Li, C.; Ramana, C.V. Interfacial Phase Modulation-Induced Structural Distortion, Band Gap Reduction, and Nonlinear Optical Activity in Tin-Incorporated Ga<sub>2</sub>O<sub>3</sub>. *J. Phys. Chem. C* **2021**, *125*, 20468–20481. [[CrossRef](#)]
33. Eliwi, A.A.; Byranvand, M.M.; Fassel, P.; Khan, M.R.; Hossain, I.M.; Frericks, M.; Ternes, S.; Abzieher, T.; Schwenzer, J.A.; Mayer, T.; et al. Optimization of SnO<sub>2</sub> electron transport layer for efficient planar perovskite solar cells with very low hysteresis. *Mater. Adv.* **2022**, *3*, 456–466. [[CrossRef](#)]
34. Mo, H.; Chen, Q.; Wang, D.; Guo, W.; Cheng, D.; Sha, Y.; Curry, R.J. Laser processing of Li-doped mesoporous TiO<sub>2</sub> for ambient-processed mesoscopic perovskite solar cells. *J. Mater. Chem. C* **2024**, *12*, 2025–2036. [[CrossRef](#)]
35. Peter Amalathas, A.; Landová, L.; Conrad, B.; Holovský, J. Concentration-Dependent Impact of Alkali Li Metal Doped Mesoporous TiO<sub>2</sub> Electron Transport Layer on the Performance of CH<sub>3</sub>NH<sub>3</sub>PbI<sub>3</sub> Perovskite Solar Cells. *J. Phys. Chem. C* **2019**, *123*, 19376–19384. [[CrossRef](#)]
36. Hoang Huy, V.P.; Nguyen, T.M.H.; Bark, C.W. Recent Advances of Doped SnO<sub>2</sub> as Electron Transport Layer for High-Performance Perovskite Solar Cells. *Materials* **2023**, *16*, 6170. [[CrossRef](#)] [[PubMed](#)]

**Disclaimer/Publisher’s Note:** The statements, opinions and data contained in all publications are solely those of the individual author(s) and contributor(s) and not of MDPI and/or the editor(s). MDPI and/or the editor(s) disclaim responsibility for any injury to people or property resulting from any ideas, methods, instructions or products referred to in the content.